www.nature.com/scientificreports

SCIENTIFIC REPORTS

OPEN

Hierarchical Sheet-on-Sheet $ZnIn_2S_4$/g-C_3N_4 Heterostructure with Highly Efficient Photocatalytic H_2 production Based on Photoinduced Interfacial Charge Transfer

Received: 24 September 2015
Accepted: 09 December 2015
Published: 12 January 2016

Zhenyi Zhang, Kuichao Liu, Zhiqing Feng, Yanan Bao & Bin Dong

We have realized *in-situ* growth of ultrathin $ZnIn_2S_4$ nanosheets on the sheet-like g-C_3N_4 surfaces to construct a "sheet-on-sheet" hierarchical heterostructure. The as-synthesized $ZnIn_2S_4$/g-C_3N_4 heterojunction nanosheets exhibit remarkably enhancement on the photocatalytic activity for H_2 production. This enhanced photoactivity is mainly attributed to the efficient interfacial transfer of photoinduced electrons and holes from g-C_3N_4 to $ZnIn_2S_4$ nanosheets, resulting in the decreased charge recombination on g-C_3N_4 nanosheets and the increased amount of photoinduced charge carriers in $ZnIn_2S_4$ nanosheets. Meanwhile, the increased surface-active-sites and extended light absorption of g-C_3N_4 nanosheets after the decoration of $ZnIn_2S_4$ nanosheets may also play a certain role for the enhancement of photocatalytic activity. Further investigations by the surface photovoltage spectroscopy and transient photoluminescence spectroscopy demonstrate that $ZnIn_2S_4$/g-C_3N_4 heterojunction nanosheets considerable boost the charge transfer efficiency, therefore improve the probability of photoinduced charge carriers to reach the photocatalysts surfaces for highly efficient H_2 production.

Photocatalytic H_2 production through water splitting or reduction has received great attention in recent years, since it offers an economical and environmentally friendly strategy to convert solar energy into preservable chemical fuels for mitigating the excessive consumption of non-sustainable fossil fuels such as coal, petroleum and natural gas[1–4]. To date, various kinds of UV- or visible-response semiconductors, such as TiO_2, ZnO, Cu_2O, CdS, and so forth, have been developed as photocatalysts for H_2 production due to their suitable band potential and catalytic functions[5–10]. Besides these traditional semiconductor photocatalysts, a large number of semiconductive materials, including metal-organic frameworks (MOFs), polyoxometalate (POM), and metal free compounds, are also being introduced as potential candidates for the new generation of photocatalysts to fulfill the photocatalytic water reduction and oxidation[11–14]. Among them, the two-dimensional (2D) layered polymer, graphitic carbon nitride (g-C_3N_4), is considered as the most promising visible-light-active photocatalyst because of its unique electronic structure, high stability, nontoxic nature, and low cost[15–17]. However, the photocatalytic activity on H_2 production over single-component g-C_3N_4 so far is unsatisfactory due to its limited surface areas, poor light-harvesting efficiency and fast recombination of photoinduced charge carriers[15,17]. To overcome the above drawbacks, much effort has been devoted to the construction of multi-component heterostructural photocatalysts through coupling other visible-active semiconductor with g-C_3N_4 nanosheets, in which the heterogeneous interfaces can effectively assist the photoinduced charge-carriers migration and hinder these charge-carriers recombination to enhance the photocatalytic efficiency[18–24]. Moreover, the surface structures and light-harvesting

Key Laboratory of New Energy and Rare Earth Resource Utilization of State Ethnic Affairs Commission, School of Physics and Materials Engineering, Dalian Nationalities University, 18 Liaohe West Road, Dalian 116600, P. R. China. Correspondence and requests for materials should be addressed to B.D. (email: dong@dlnu.edu.cn)

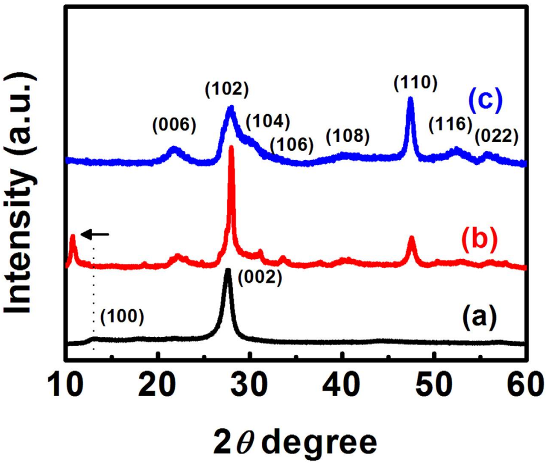

Figure 1. XRD patterns of the as-synthesized samples: (**a**) g-C_3N_4 nanosheets; (**b**) 15 wt% $ZnIn_2S_4$/g-C_3N_4 heterojunction nanosheets; (**c**) $ZnIn_2S_4$ nanosheets.

behavior can be also promoted through tailoring the secondary nanostructures of heterostructural photocatalysts[25–27]. Therefore, design and architecture of g-C_3N_4-based heterostructural photocatalysts with the matchable bandgap, desired component, and hierarchical nanostructures is still the hot topics in the field of solar-to-fuels conversion.

As an important ternary chalcogenide semiconductor, hexagonal phase $ZnIn_2S_4$ with 2D layered structure and narrow bandgap has been extensively investigated in photocatalysis, especially serving as the photosynergistic components in heterojunction photocatalysts to enhance the photocatalytic efficiency for H_2 production[28–32]. In the viewpoint of band structure, the bandgap of $ZnIn_2S_4$ ($E_g^{ZnIn_2S_4} = \sim 2.6$ eV) is smaller than that of g-C_3N_4 ($E_g^{C_3N_4}$ ~2.8 eV) while the conduction band (CB) of $ZnIn_2S_4$ ($E_{CB}^{ZnIn_2S_4} = -1.0$ V) is higher than that of g-C_3N_4 ($E_{CB}^{C_3N_4} = -1.1$ V)[15,17,28,33]. Accordingly, when integrating of $ZnIn_2S_4$ nanostructure with g-C_3N_4 nanosheets, a "type I" heterojunction would be formed in their interface, meaning that the CB and valence band (VB) positions of g-C_3N_4 straddle those of $ZnIn_2S_4$. As such, the $ZnIn_2S_4$ can be seemed as a "charge sink" to accept the photoinduced charge carriers from adjacent g-C_3N_4, leading to the improvement of charge separation on g-C_3N_4 and thereby enhancing its photocatalytic activity. On the other hand, the 2D sheet-like $ZnIn_2S_4$ nanostructures could be easily anchored onto the active or flexible 2D substrates, such as F-doped SnO_2 (FTO) thin film and reduced graphene oxide (RGO) nanosheets, to form the "sheet-on-sheet" type heterostructure. This kind of hierarchical nanostructure usually exhibits a high surface area, strong light harvesting, and efficient charge mobility due to its unique structure advantages[25,26,29,31,33,34]. The above analysis implies that once the $ZnIn_2S_4$ nanosheets combine with g-C_3N_4 nanosheets, a significant enhancement on photocatalytic H_2 production may be realized through synergistic promotion on the inner charge carriers and outer hierarchical structures. However, little effort has been donated to the synthesis of $ZnIn_2S_4$/g-C_3N_4 heterostructure toward the highly efficient photocatalytic H_2 production. Herein, we report a novel kind of "sheet-on-sheet" heterostructure synthesized through *in-situ* growth of ultrathin $ZnIn_2S_4$ nanosheets onto g-C_3N_4 nanosheets surfaces. After introducing the $ZnIn_2S_4$ nanosheets, the specific surface area of g-C_3N_4 nanosheets is obviously promoted, resulting in providing the more active sites for the photoreaction. Furthermore, the intimate contacted interface between the $ZnIn_2S_4$ and g-C_3N_4 nanosheets facilitates the photoinduced charge-carriers transfer from g-C_3N_4 to $ZnIn_2S_4$ based on the heterojunction effect. By taking of the above features, the as-synthesized $ZnIn_2S_4$/g-C_3N_4 heterojunction nanosheets exhibit a significantly enhanced visible-light photocatlaytic H_2 production performance as compared to the single component of $ZnIn_2S_4$ or g-C_3N_4 nanosheets.

Results

X-ray diffraction (XRD) patterns of the as-synthesized samples are shown in Fig. 1. Two pronounced diffraction peaks appear at 13.1° and 27.4° for g-C_3N_4 nanosheets, reflecting to the periodic structure of intra-planar tri-s-triazine packing as the (100) peak, and the interlayer stacking of conjugated aromatic structures as the (002) peak for graphitic materials, respectively[11,15,17]. The diffraction peaks of $ZnIn_2S_4$ nanosheets can be perfectly indexed as a pure hexagonal phase of $ZnIn_2S_4$ (JCPDS No. 65–2023)[28,29,31]. In the case of $ZnIn_2S_4$/g-C_3N_4 heterojunction nanosheets, the XRD pattern shows diffraction peaks of both $ZnIn_2S_4$ and g-C_3N_4 nanosheets, while the feature peaks of $ZnIn_2S_4$ (27.7°) and g-C_3N_4 (27.4°) are very close and overlap with each other. Note that the diffraction peaks of $ZnIn_2S_4$ nanosheets are very weak. This phenomenon may be ascribed to two reasons: (1) the ultrathin 2D nanostructure of $ZnIn_2S_4$, leading to the ultra-small size in its c-axis orientation[31]; (2) the low content of $ZnIn_2S_4$ component in the heterostructure[25]. Besides, after introducing the $ZnIn_2S_4$ by hydrothermal method, the (100) diffraction peak of g-C_3N_4 becomes more intense, and its position shifts toward the lower diffraction angle (10.8°) (Figure S1). This reveals that some metal ions from $ZnIn_2S_4$ surfaces may be connected with the g-C_3N_4 through the lone-pair electrons of nitrogen in the "nitrogen pots", thus leading to enlarging the intra-planar separation of ordered tri-s-triazine packing[21,22,35]. Moreover, some weak peaks corresponded to the

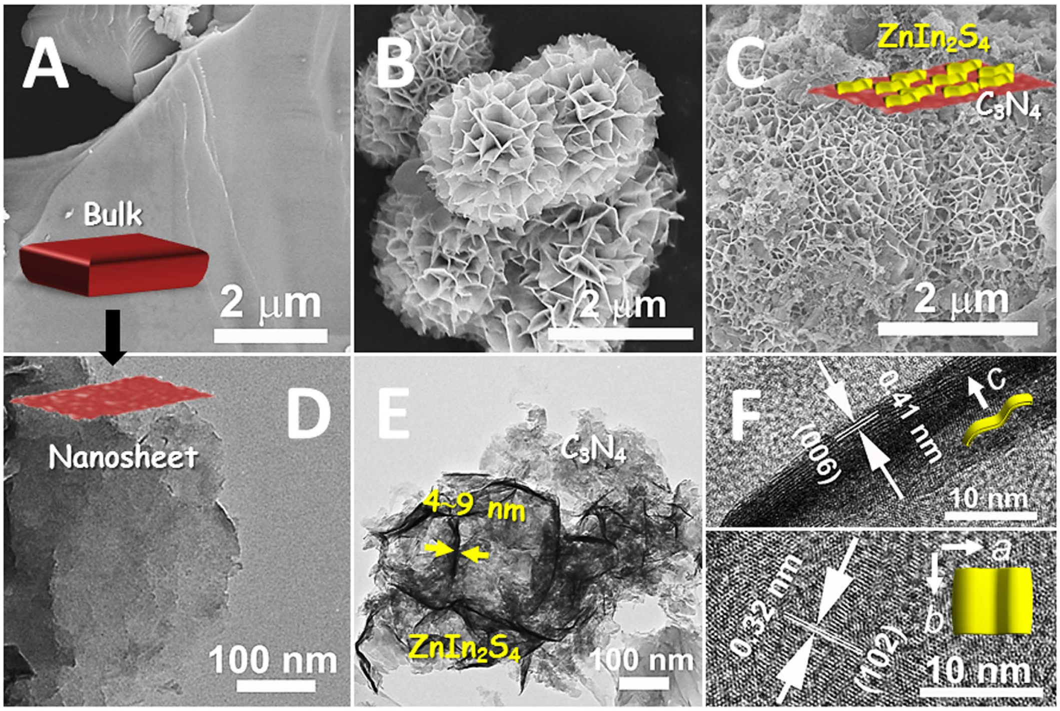

Figure 2. SEM images of (**A**) bulk g-C_3N_4, (**B**) $ZnIn_2S_4$ nanosheets, and (**C**) $ZnIn_2S_4$/g-C_3N_4 heterojunction nanosheets; TEM images of (**D**) the exfoliated g-C_3N_4 nanosheet and (**E**) 15 wt% $ZnIn_2S_4$/g-C_3N_4 heterojunction nanosheets; (**F**) HRTEM images of the side view and top view of $ZnIn_2S_4$ nanosheet grown on the g-C_3N_4 nanosheets. Insets showing structure schematic diagrams of the corresponding samples.

intermediates of thermal polymerized g-C_3N_4 are also detected on the XRD pattern of $ZnIn_2S_4$/g-C_3N_4 heterojunction nanosheets, implying that a small part of g-C_3N_4 nanosheets might be further exfoliated (or reduced) into the structural units of g-C_3N_4, such as melamine, ammeline, or tri-s-triazine units, due to the longer reaction time for hydrothermal growth of $ZnIn_2S_4$ onto g-C_3N_4 nanosheets[16,36].

Scanning electron microscopy (SEM) and transmission electron microscopy (TEM) images were performed to directly observe the morphologies and structures of the $ZnIn_2S_4$/g-C_3N_4 heterojunction nanosheets in comparison with the single component of $ZnIn_2S_4$ and g-C_3N_4 nanosheets, as displayed in Fig. 2. The thermal polymerized g-C_3N_4 shows a bulk structure with smooth surfaces (Fig. 2A), which can be easily exfoliated into the wrinkled sheet-like nanostructures by the ultrasonic treatment in methanol solution (Fig. 2D). Figure 2B reveals significant aggregation of the nanosheets into microspheres with the average diameter of ~1.5 μm for the hydrothermally synthesized $ZnIn_2S_4$ sample. Interestingly, when introducing the as-fabricated g-C_3N_4 nanosheets as the substrates during the hydrothermal process, the $ZnIn_2S_4$/g-C_3N_4 heterojunction nanosheets could be achieved in the form of "sheet-on-sheet" structure (Figure S2 and Figure S3). As observed in Fig. 2C, the layered surfaces of g-C_3N_4 nanosheet are covered with the high density of secondary $ZnIn_2S_4$ nanosheets. These nanosheets with uniformly ultrathin 2D-structure are connected and even across to each other, finally forming the sheet-like networks vertically aligned on the g-C_3N_4 nanosheet surface. This kind of unique hierarchical heterostructure (65.9 $m^2 g^{-1}$) shows much higher specific-surface-area than the general sheet-like structure for pure g-C_3N_4 (12.8 $m^2 g^{-1}$), thereby providing more active sites for the photocatalytic reaction.(Figure S4) Moreover, the interspaces among interweaved $ZnIn_2S_4$ nanosheets on the g-C_3N_4 nanosheets may also boost the light-harvesting behavior of this hierarchical heterostructure though the multi-reflection processes on the incident electromagnetic waves[25,26,29]. TEM image of the $ZnIn_2S_4$/g-C_3N_4 heterojunction nanosheets further confirms that the ultrathin $ZnIn_2S_4$ nanosheets with thickness of 4～9 nm are vertically grown onto the g-C_3N_4 nanosheets surface (Fig. 2E and Figure S3). Figure 2F presents the high-resolution (HR) TEM of an individual $ZnIn_2S_4$ nanosheet on g-C_3N_4 surface, in which the lattice-fringe spacing of 0.41 nm appeared on the side view (perpendicular sheet) can be assigned to the (006) crystal plane of hexagonal $ZnIn_2S_4$, while the top view (planar sheet) image shows the interplanar distances of 0.32 nm, belonging to the *d*-spacing of (102) planes of hexagonal $ZnIn_2S_4$. In short, intimate contacted heterojunctions between $ZnIn_2S_4$ and g-C_3N_4 nanosheets are indeed constructed by the *in-situ* growth process, which may be beneficial for the photoinduced interfacial charge-transfer from g-C_3N_4 to $ZnIn_2S_4$.

Figure 3A presents the Fourier transform infrared (FT-IR) spectra of the as-synthesized $ZnIn_2S_4$/g-C_3N_4 heterojunction nanosheets along with the single $ZnIn_2S_4$ and g-C_3N_4 nanosheets for the purpose of structure comparison. The stretching vibration bands on the spectra of g-C_3N_4 nanosheets show characteristics similar to those of the reported results[13,16,21,23]. Accordingly, the peaks appeared between 1200 cm^{-1} and 1650 cm^{-1} are attributed to the stretching vibration modes of CN heterocycles. The peak located at 3200 cm^{-1} is originated to the NH stretching vibration mode, while the 811 cm^{-1} to the feature vibration mode of *s*-triazine ring unit. For the $ZnIn_2S_4$ sample, only two peaks at 1396 cm^{-1} and 1610 cm^{-1}, belonging to the surface hydroxyl groups

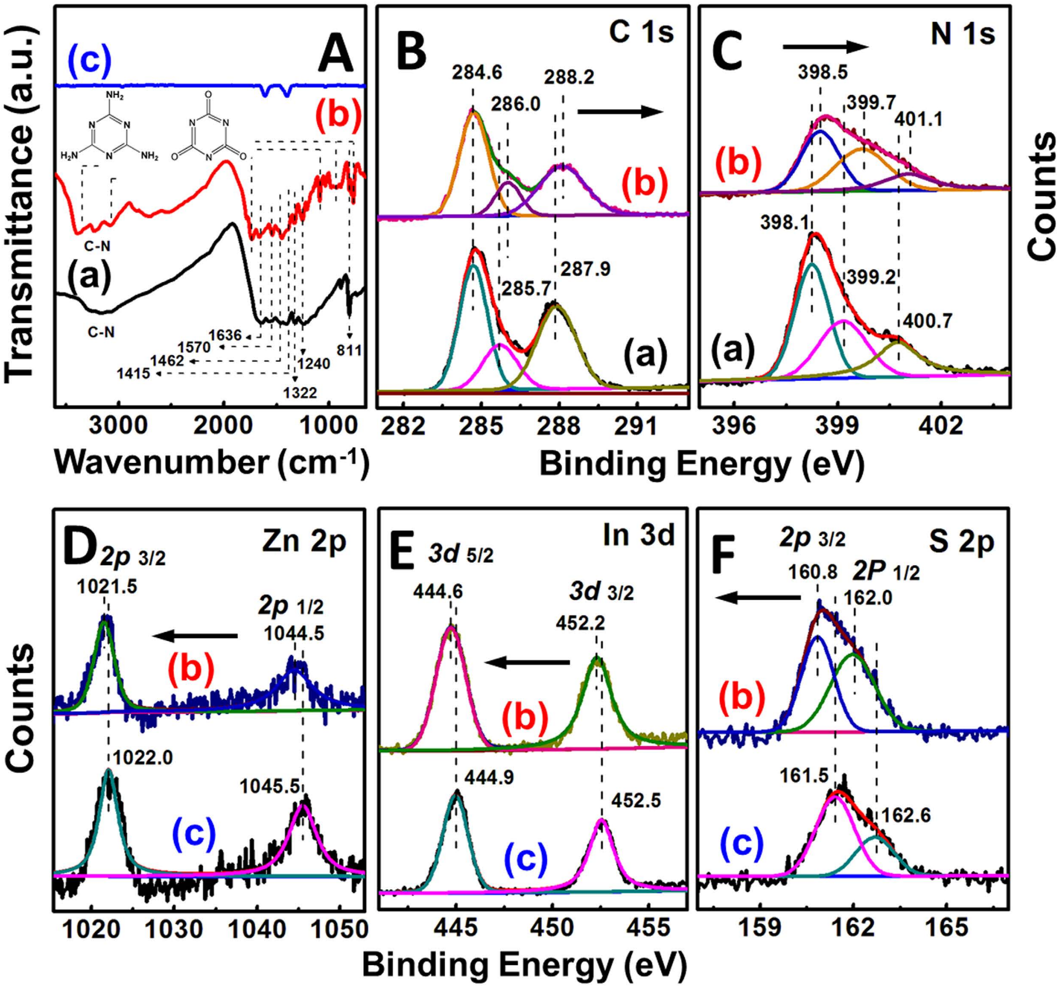

Figure 3. (**A**) FT-IR spectra of the as-synthesized samples: (a) g-C_3N_4 nanosheets, (b) 15 wt% $ZnIn_2S_4$/g-C_3N_4 heterojunction nanosheets, and (c) $ZnIn_2S_4$ nanosheets; XPS spectra of the as-synthesized samples: (**B**) C 1s core-level spectra; (**C**) N 1s core-level spectra: (a) g-C_3N_4 nanosheets, (b) 15 wt% $ZnIn_2S_4$/g-C_3N_4 heterojunction nanosheets; (**D**) Zn 2p core-level spectra; (**E**) In 3d core-level spectra; (**F**) S 2p core-level spectra: (b) 15 wt% $ZnIn_2S_4$/g-C_3N_4 heterojunction nanosheets, and (c) $ZnIn_2S_4$ nanosheets.

and absorbed water molecules, can be observed on the FT-IR spectrum[25]. After the growth of $ZnIn_2S_4$ nanosheets onto g-C_3N_4 surfaces, the heterojunction nanosheets show the typical stretching vibration modes of both $ZnIn_2S_4$ and g-C_3N_4 nanosheets. Besides, a series of new vibration bands can be detected simultaneously on the spectrum of $ZnIn_2S_4$/g-C_3N_4 nanosheets, which are in agreement with the vibration bands of melamine and/or ammeline[16,36]. This further suggests that during the long-time hydrothermal process, a few number of g-C_3N_4 nanosheets were exfoliated (or reduced) into the sub-structures of g-C_3N_4. To study in-depth the chemical configurations of the as-synthesized samples, the X-ray photoelectron spectroscopy (XPS) analyses were performed. As observed in Fig. 3B, three main peaks with the binding energies at 284.6 eV, 285.7 eV, and 287.9 eV can be found on the C 1s core-level spectrum of g-C_3N_4 nanosheets, which are assigned to sp^2 C-C bonds of graphitic carbon, sp^3-coordinated carbon bonds, and sp^2-bonded carbon (N-C = N) of the s-triazine rings, respectively[17,21]. The binding energy for the C 1s peak at 284.6 eV can be attributed to the adventitious carbon species on the samples and the carbon-containing contaminants, which was used as the reference for calibration. The N 1s signal of g-C_3N_4 nanosheets also shows three feature peaks, corresponding to the sp^2-bonded N (C-N = C) (398.1 eV), tertiary nitrogen N-$(C)_3$ groups (399.2 eV), and amino groups (C-N-H) (400.7 eV)[17,21]. Investigations found that the relative intensity of the peaks relating to the N-C = N and C-N = C groups of g-C_3N_4 nanosheets are decreased after hydrothermal treatment for a long time, indicating that some of the tri-s-triazine units of g-C_3N_4 were distorted during this process. Meanwhile, when introducing the $ZnIn_2S_4$ nanosheets onto g-C_3N_4 nanosheets to form the heterojunction, both the C 1s and N 1s characteristic signals of g-C_3N_4 nanosheets shift slightly toward the higher binding energy side. On the contrary, the binding energies of Zn *2p* (1022.0 eV for $2p_{3/2}$ and 1045.5 eV for $2p_{1/2}$), In *3d* (444.9 eV for $3d_{5/2}$ and 452.5 eV for $3d_{3/2}$), and S *2p* (161.5 eV for $2p_{3/2}$ and 162.6 eV for $2p_{1/2}$) for the $ZnIn_2S_4$/g-C_3N_4 heterojunction nanosheets are a little lower than the corresponding values for the pure $ZnIn_2S_4$ nanosheets[25,29,31], as shown in Fig. 3D–F. The binding energy shifts λfor the heterojunction components could be explained by a strong interaction between $ZnIn_2S_4$ and g-C_3N_4 nanosheets[21,37–39]. Theoretically, the enhancement

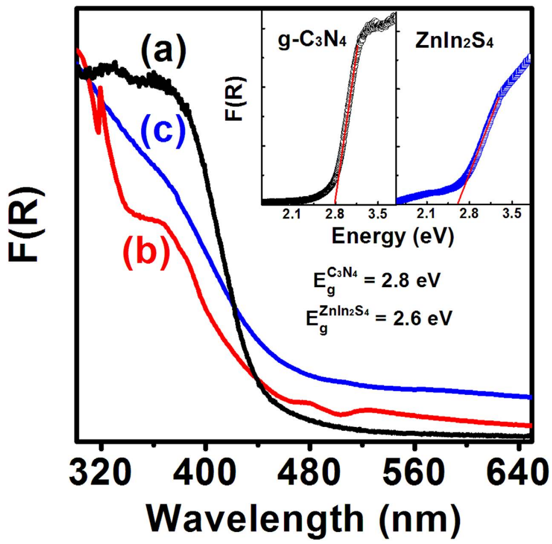

Figure 4. UV-Vis absorption spectra of the as-synthesized samples: (**a**) g-C_3N_4 nanosheets, (**b**) 15 wt% $ZnIn_2S_4$/g-C_3N_4 heterojunction nanosheets, and (**c**) $ZnIn_2S_4$ nanosheets; insets showing the plots of the F(R) versus energy for the g-C_3N_4 and $ZnIn_2S_4$ nanosheets.

of binding energy means the weakened electron screening effect caused by the decreased electron concentration, while the increase in electron concentration leads to the decrease of binding energy due to the promoted electron screening effect. Thus, in this case, it is reasonable to conclude that the higher and lower binding energy shifts are ascribed to the decreased electron concentration of g-C_3N_4 nanosheets and increased electron concentration of $ZnIn_2S_4$ nanosheets due to the strong interaction between the g-C_3N_4 to $ZnIn_2S_4$ nanosheets based on the interfacial charge transfer.

The optical properties of the as-synthesized samples were investigated through UV-vis absorption spectra which converted from the corresponding diffuse reflectance (DR) spectra by means of the Kubelka-Munk function. As shown in Fig. 4, the absorption edges of g-C_3N_4 and $ZnIn_2S_4$ nanosheets appears at ~443 and ~476 nm, corresponding to the band energies of ~2.8 and ~2.6 eV, respectively. These values are consistent with the reported values of g-C_3N_4 and $ZnIn_2S_4$ nanosheets[15,17–19,28,33,34]. In the case of $ZnIn_2S_4$/g-C_3N_4 heterojunction nanosheets, two obvious absorption bands ascribed to the characteristic absorption of g-C_3N_4 and $ZnIn_2S_4$ nanosheets can be found on the absorption curve of Fig. 4b. Moreover, the absorption peaks of $ZnIn_2S_4$ nanosheets become more intense with increase of $ZnIn_2S_4$ content in the heterojunction nanosheets (Figure S5), further confirming that the $ZnIn_2S_4$/g-C_3N_4 heterojunction nanosheets with controllable component contents were obtained.

Discussion

Photocatalytic H_2 production activities of the as-synthesized samples were evaluated under visible light ($\lambda > 400$ nm) irradiation by using triethanolamine (TEOA) as the sacrificial reagent to quench the photoinduced holes. The H_2 production rates of pure g-C_3N_4 nanosheets, pure $ZnIn_2S_4$ nanosheets, and $ZnIn_2S_4$/g-C_3N_4 heterojunction nanosheets with various $ZnIn_2S_4$ ratios are summarized in Fig. 5A, in which the heterojunction nanosheets show the enhanced H_2 production rates as compared to the single heterojunction components. It implies that *in-situ* growth of $ZnIn_2S_4$ nanosheets onto g-C_3N_4 nanosheets could noticeably improve the photocatalytic activities on H_2 production. Even with only 2.5 wt% $ZnIn_2S_4$ nanosheets, the heterojunction nanosheet displays a H_2 production rate of 5.2 μmol h^{-1}, which is more than 6 times higher than that of pure g-C_3N_4 nanosheets (0.8 μmol h^{-1}). The poor photoactivity of g-C_3N_4 nanosheets for the H_2 production is mainly ascribed to its limited light-harvesting efficiency and fast recombination of photoinduced charge carriers[18,19]. The optimal photocatalytic activity was achieved on 15 wt% $ZnIn_2S_4$ with a H_2 production rate of 14.1 μmol h^{-1}. This value is ~17.6 times higher than that of pure g-C_3N_4 nanosheets and even nearly 4 times higher that of the pure $ZnIn_2S_4$ nanosheets. Accordingly, the apparent quantum efficiency of this optimal sample is estimated as 0.28% under irradiation at 420 nm. Note that only 5 mg of 15 wt% $ZnIn_2S_4$/g-C_3N_4 heterojunction nanosheets was used for H_2 production in our work. However, when the $ZnIn_2S_4$ content is higher than 15 wt%, a further increase in $ZnIn_2S_4$ content (20 wt%) leads to a rapid decrease in the photocatalytic activity for H_2 production. This photoactivity reduction can be attributed to the increased opacity (so-called shield effect), resulting in a decrease of irradiation passing through the suspension photoreaction solution[21,25,29,31,40,41]. As observed in Fig. 5B, the significant enhancement of photocatalytic activity for the heterojunction sample can be further confirmed by the time-dependent H_2 production behaviors. It could be found that the H_2 production amounts linearly increases with the irradiation time. After visible light irradiation for 2h, the H_2 production yield of 15 wt% $ZnIn_2S_4$-decorated g-C_3N_4 nanosheet could reach 28.2 μmol, which is greatly superior to the pure g-C_3N_4 and $ZnIn_2S_4$ nanosheets. The enhanced photoactivity on H_2 production could be explained by two main reasons: (1) the reduced recombination process of photoinduced charge carriers on g-C_3N_4 and increased amount of charge carriers on $ZnIn_2S_4$ based on the interfacial charge transfer; (2) the higher specific-surface-area and enhanced light absorption for

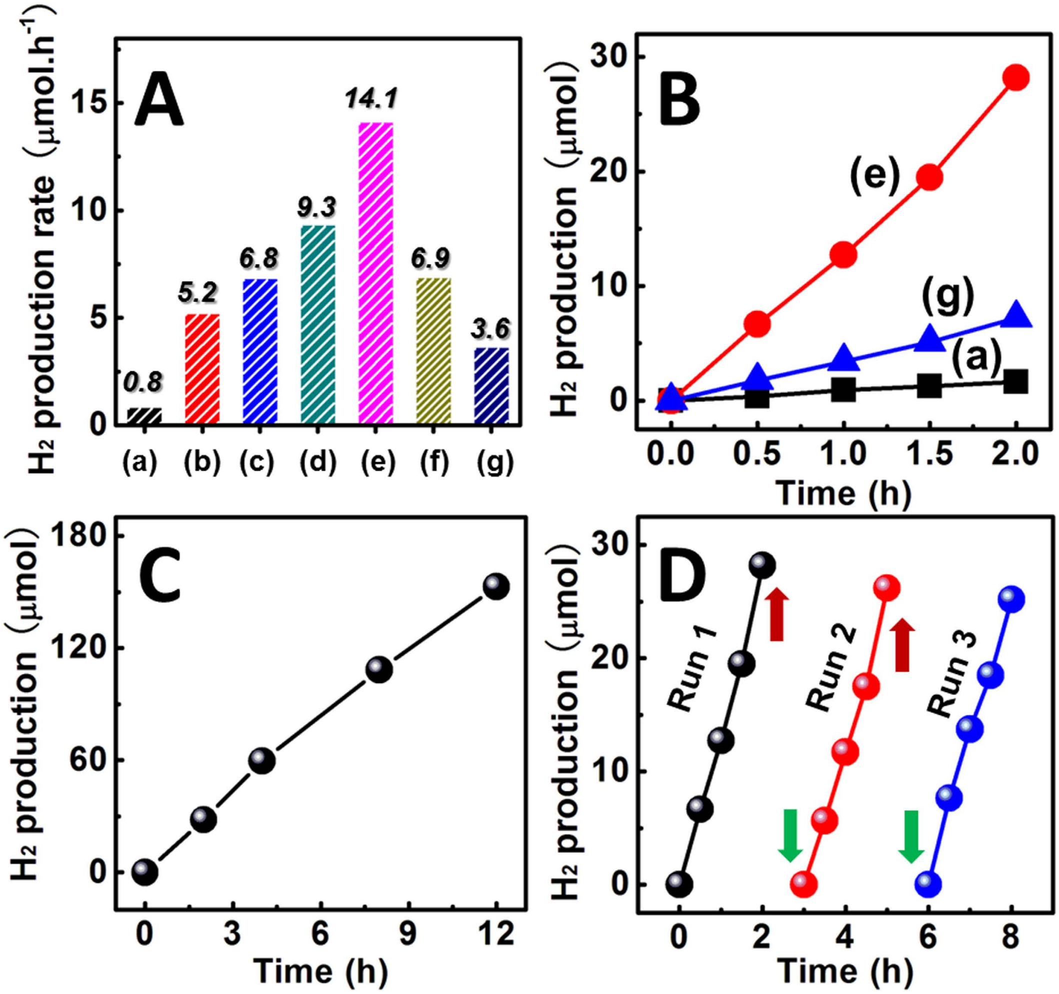

Figure 5. (**A**) Photocatalytic H_2 production under visible light irradiation over (a) g-C_3N_4 nanosheets; (e) 15 wt% $ZnIn_2S_4$/g-C_3N_4 heterojunction nanosheets, and (g) $ZnIn_2S_4$ nanosheets; (**B**) comparison of visible-light-driven H_2 production rate over different samples: (a) g-C_3N_4 nanosheets, (b) 2.5 wt%, (c) 5 wt%, (d) 10 wt%, (e) 15 wt%, (f) 20 wt% $ZnIn_2S_4$/g-C_3N_4 heterojunction nanosheets, and (g) $ZnIn_2S_4$ nanosheets; (**C**) photocatalytic H_2 production curve with prolonged irradiation time over 15 wt% $ZnIn_2S_4$/g-C_3N_4 heterojunction nanosheets; (**D**) cycling test of photocatalytic H_2 production over 15 wt% $ZnIn_2S_4$/g-C_3N_4 heterojunction nanosheets.

the unique "sheet-on-sheet" heterostructure as aforementioned. However, it should be point out that in comparison with the pure $ZnIn_2S_4$ nanosheets (132.0 $m^2 g^{-1}$), the heterojunction nanosheets (65.9 $m^2 g^{-1}$) shows the lower specific-surface-area, but the higher photoactivity. Meanwhile, the g-C_3N_4 nanosheets treated by the hydrothermal process in the absence of $ZnIn_2S_4$ precursor show a lower photocatalytic H_2 production rate (0.41 μmol/h) as compared to the pure (untreated) g-C_3N_4 nanosheets (Figure S6), because of the poor photoactivities of the exfoliation or reduction of g-C_3N_4 with the ultra-small structures, such as melamine, ammeline, or tri-s-triazine units[16,36]. These observations also the indirect evidence that the dynamics process of photoinduced charge transfer occurring on the interface between the $ZnIn_2S_4$ and g-C_3N_4 nanosheets may be crucial to the photocatalytic H_2 production activities of heterojunction nanosheets. At low $ZnIn_2S_4$ content, a well dispersion of $ZnIn_2S_4$ nanosheets on the g-C_3N_4 nanosheets could be formed. In this way, the increase of $ZnIn_2S_4$ content would induce more $ZnIn_2S_4$ nanosheets assembled onto the g-C_3N_4 surface, which generates larger contact area between the $ZnIn_2S_4$ and g-C_3N_4 nanosheets, thereby allowing more efficient interfacial charge transfer. However, excess $ZnIn_2S_4$ loading causes considerable reduction of light absorption for the covered g-C_3N_4, and decreases its excitation process for interfacial charge transfer. Therefore, a balance would be built between $ZnIn_2S_4$ loading amount and $ZnIn_2S_4$/g-C_3N_4 contact area, which can maximize the photocatalytic H_2 production for the heterojunction nanosheets. Through the sequential remediation of heterojunction components, we concluded an optimal loading of 15 wt% $ZnIn_2S_4$ onto g-C_3N_4, which exhibited the highest photocatalytic activity in our work.

Besides, this optimal $ZnIn_2S_4$/g-C_3N_4 heterojunction nanosheets also shows fairly stable photoactivity for H_2 production. In Fig. 5C, the H_2 production rate remains consistent even at the prolonged time period for 12 h. Meanwhile, the recycling ability for the 15 wt% $ZnIn_2S_4$/g-C_3N_4 heterojunction nanosheets was further studied by performing a three-run test of photocatalytic H_2 production. Figure 5D shows that no notable decreases

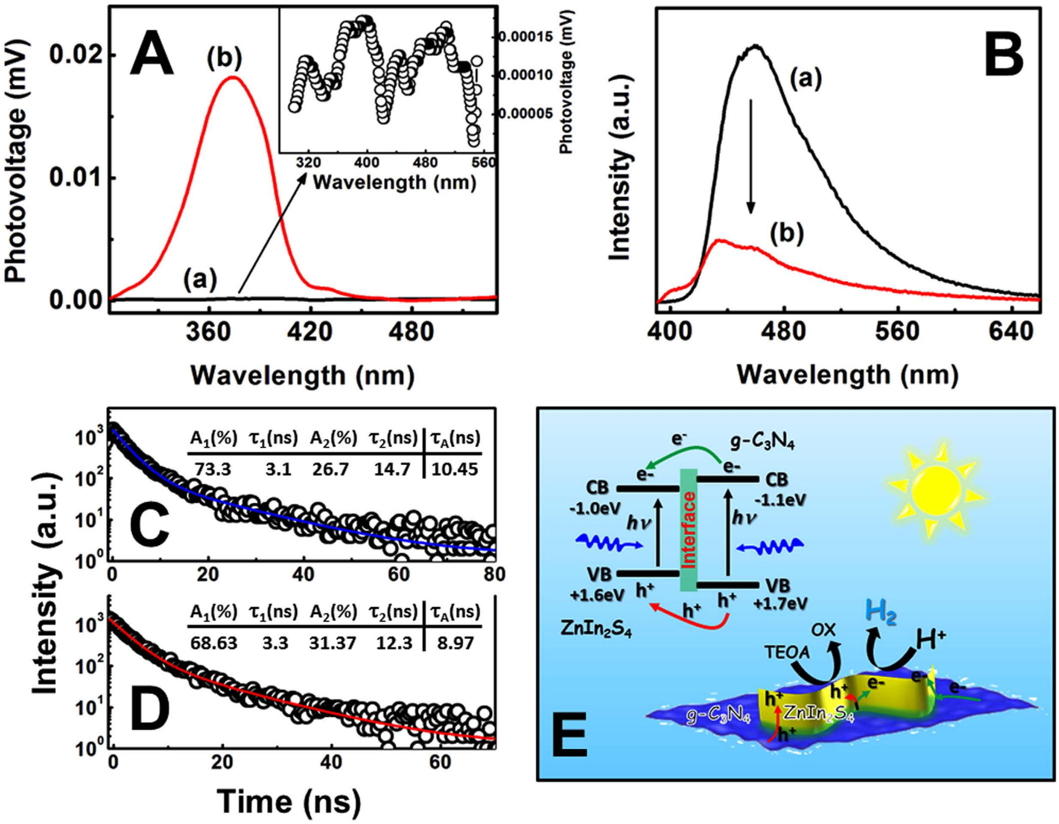

Figure 6. (**A**) SPS of the as-synthesized samples: (a) g-C_3N_4 nanosheets, (b) 15 wt% $ZnIn_2S_4$/g-C_3N_4 heterojunction nanosheets; (**B**) steady-state PL spectra of (a) g-C_3N_4 nanosheets and (b) 15 wt% $ZnIn_2S_4$/g-C_3N_4 heterojunction nanosheets; Time-resolved transient PL decay of (**C**) g-C_3N_4 nanosheets and (**D**) 15 wt% $ZnIn_2S_4$/g-C_3N_4 heterojunction nanosheets; (**E**) schematic diagram showing the photoinduced charge transfer in the interface between $ZnIn_2S_4$ and g-C_3N_4 nanosheets.

of H_2 evolution were detected during the three-run test, powerfully verifying the good stability of 15 wt% $ZnIn_2S_4$/g-C_3N_4 heterojunction nanosheets for using as the photocatalysts.

To provide more evidence on the photoinduced charge transfer occurring in the heterojunction interface, the surface photovoltage spectroscopy (SPS) and photoluminescence (PL) spectroscopy of $ZnIn_2S_4$/g-C_3N_4 heterojunction nanosheets were investigated in comparison with those of pure g-C_3N_4 nanosheets. As shown in the inset of Fig. 6A, a poor response appears on the SPS curve of pure g-C_3N_4 nanosheets, indicating very low efficiency on the photovoltaic conversion. However, the photon absorption and conversion processes have been proven by the photoelectrochemistry in our previous work[42]. Thus, the low photovoltage of g-C_3N_4 nanosheets can be attributed to the Schottky interface contact between the g-C_3N_4 and ITO glass in the absence of electrolyte, which leads to the limited electron transfer process from the g-C_3N_4 to ITO glass electrode. After decoration of $ZnIn_2S_4$ onto g-C_3N_4 nanosheets, the SPS signal in the region from 300 to 450 nm is remarkably enlarged, suggesting the promoted charge generation and separation based on the semiconductor heterojunction effect. This phenomenon can be further understood through the steady-state and transient PL spectroscopy. In Figre 6B, the pure g-C_3N_4 nanosheet shows a strong emission peak with the center at ~450 nm. However, as compared to the g-C_3N_4 nanosheets, the emission process of $ZnIn_2S_4$/g-C_3N_4 heterojunction nanosheets suppresses significantly, revealing either the faster migration process with the shorter lifetime or the slower recombination process with the longer lifetime for the photoinduced charge carriers. To shed more light on this issue, we tried to fit the time-resolved transient PL spectroscopy based on the multi-exponential kinetics function expressed as follow[43]:

$$\mathrm{I}(t) = A_1 \cdot \exp(-t/\tau_1) + A_2 \cdot \exp(-t/\tau_2) \quad (1)$$

where τ_1 and τ_2 are the fluorescent lifetime, and A_1, and A_2 are the corresponding amplitudes. As listed in the insets of Fig. 6C,D, the short lifetime component for τ_1 is originated from the nonradiative recombination of charge-carriers in the defect states of g-C_3N_4, while the longer lifetime component for τ_2 is caused by the free excitons recombination in the g-C_3N_4 body[12,21,34,42]. In the case of $ZnIn_2S_4$/g-C_3N_4 heterojunction nanosheets, the emission lifetime for the component τ_1(3.3 ns) is longer than the corresponding lifetime of g-C_3N_4 nanosheets (3.1 ns), while its component τ_2 (12.3 ns) is shorter than the component for g-C_3N_4 nanosheets (14.7 ns). To gain further understanding on this phenomenon, the average emission lifetimes, relating to the overall emission decay behaviors of the samples, were also evaluated through the following equation[44]:

$$\tau_A = \frac{A_1 \cdot \tau_1^2 + A_2 \cdot \tau_2^2}{A_1 \cdot \tau_1 + A_2 \cdot \tau_2} \tag{2}$$

It is clearly that after loading the $ZnIn_2S_4$ nanosheets, the average lifetime of g-C_3N_4 nanosheets is shorten from 10.45 ns to 8.97 ns. The combination of decreased emission lifetime and quenched PL indicates the emergence of a nonradiative pathway from the electron transfer between $ZnIn_2S_4$ and g-C_3N_4 nanosheets[45]. According to the energy band structures of these semiconductors (Fig. 6E), it could be deduced that the photoinduced electrons transfer from the conduction band (CB) of g-C_3N_4 to the CB of $ZnIn_2S_4$ nanosheets. This assumption is in agreement with the emission quenching phenomenon of g-C_3N_4 nanosheets after decorating the $ZnIn_2S_4$ nanosheets. The rate constant for the interfacial electron-transfer (k_{et}) can be estimated by the expression[46]:

$$k_{et}(g - C_3N_4 \rightarrow ZnIn_2S_4) = \frac{1}{\langle \tau_A \rangle_{(ZnIn_2S_4/g-C_3N_4)}} - \frac{1}{\langle \tau_A \rangle_{(g-C_3N_4)}} \tag{3}$$

Obviously, the k_{et} value is approximately ~$1.6 \times 10^7\ S^{-1}$. As illustrated in Fig. 6E, the CB and valence band (VB) positions of g-C_3N_4 straddle those of $ZnIn_2S_4$, forming the "type I" heterojunction interface. When this heterojunction is excited by visible light with the photon energy higher or equal to the band gaps of both $ZnIn_2S_4$ and g-C_3N_4 nanosheets, the photoinduced electrons and holes of g-C_3N_4 nanosheets would move to the CB and VB of $ZnIn_2S_4$ nanosheets, respectively. As such, the recombination process on the photoinduced charge carriers of g-C_3N_4 could be suppressed effectively by the photosynergistic effect of $ZnIn_2S_4$/g-C_3N_4 heterojunction. Accordingly, the amount of photoinduced charge carriers on $ZnIn_2S_4$ is remarkably increased based on the photoinduced interfacial charge transfer. During the photocatalytic H_2 production process, the photoinduced electrons accumulated on the CB of $ZnIn_2S_4$ could initiate the catalytic proton reduction to H_2. Accordingly, the photoinduced holes transfer from the VB of g-C_3N_4 to the VB of $ZnIn_2S_4$ were quenched by the sacrificial reagent of TEOA (or directly quenched by the sacrificial reagent on the VB of g-C_3N_4). In this way, the effective charge transfer at the interface between the $ZnIn_2S_4$ and g-C_3N_4 nanosheets results in the enhanced photocatalytic activity on H_2 production.

In summary, a series of $ZnIn_2S_4$/g-C_3N_4 heterojunction nanosheets with various contents of $ZnIn_2S_4$ have been successfully synthesized through *in-situ* growth of ultrathin $ZnIn_2S_4$ nanosheets onto g-C_3N_4 nanosheets fabricated by a traditional thermal polymerization and followed ultrasonic dispersion method. The unique "sheet-on-sheet" heterostructure obtained by vertically loading $ZnIn_2S_4$ nanosheets onto the g-C_3N_4 nanosheets surfaces leads to the enlarged reactive sites and enhanced light absorption ability. More importantly, the formation of "type I" heterojunction can effectively suppress the photoinduced charge recombination of g-C_3N_4 through the interfacial charge transfer, as evidenced by the electron microscopic analyses, steady-state and time-resolved transient photoluminescence decay investigations. As a result, the $ZnIn_2S_4$/g-C_3N_4 heterojunction nanosheets exhibited considerable enhancement on the photocatalytic activity for H_2 production as compared the single component nanosheets. It is believed that our study provides a promising strategy to develop the new generation of hierarchical heterostructure photocatalysts for highly efficient solar-to-fuels conversion and environmental remediation.

Methods

Materials synthesis. The graphitic carbon nitride (g-C_3N_4) was obtained by a traditional thermal polymerization method. 10 g of melamine powder was grinded for 60 min in a mortar and then transferred to an alumina crucible with a cover. Afterward, the crucible was heated to 550 °C with a rising rate of 20 °C min^{-1} and kept for 2 h at the required temperature under semiclosed environment, resulting in the bulk g-C_3N_4 with faint-yellow color. $ZnIn_2S_4$/g-C_3N_4 heterojunction nanosheets were synthesized by *in-situ* growth of ultrathin $ZnIn_2S_4$ nanosheets onto g-C_3N_4 nanosheets through a facile hydrothermal method. In a typical procedure, 600 mg of as-synthesized bulk g-C_3N_4 was grinded to fine powder and then added into 20 ml of methanol. After ultrasonic treatment for 2 h, the bulk g-C_3N_4 was exfoliated into thin nanosheets which was then collected and washed by using centrifugation-redispersion with deionized water. Subsequently, these exfoliated g-C_3N_4 nanosheets was resuspended into 20 ml of premade aqueous solution consisting of 0.2125 mmol of $Zn(CH_3COO)_2 \cdot 2H_2O$, 0.425 mmol of $In(NO_3)_3 \cdot 6H_2O$, and 1.7 mmol of L-cysteine. After being ultrasonically treated for 30 min, this mixture was transferred into a Teflon-lined stainless steel autoclave with a capacity of 25 mL. Afterward, the autoclave was sealed and maintained at 180 °C for 12 h in an electric oven. When natural cooling the autoclave to room temperature, the yellow-green suspension was collected, washed with ethanol and deionized water for several times, and finally dried in an electric oven at 60 °C for a night. Thus, the 15 wt% $ZnIn_2S_4$/g-C_3N_4 heterojunction nanosheets were synthesized. The pure $ZnIn_2S_4$ nanosheets were fabricated by the same hydrothermal conditions in the absence of the g-C_3N_4 nanosheets substrates. Meanwhile, to achieve the optimal photocatalytic activity, the $ZnIn_2S_4$/g-C_3N_4 heterojunction nanosheets with different $ZnIn_2S_4$ loading amount were also synthesized using the similar route by adjusting the concentrations of hydrothermal precursor solution in the same component ratios. In order to further prove that the enhanced photocatalytic activity of $ZnIn_2S_4$/g-C_3N_4 nanosheets is due to the heterojunction effect, another control sample were fabricated through hydrothermal treatment of pure g-C_3N_4 nanosheets in the absence of the above $ZnIn_2S_4$ precursors.

Characterization methods. X-ray diffraction (XRD) patterns of the as-synthesized samples were measured by a Shimadzu XRD-6000 X-ray diffractometer with a Cu Kα line of 0.1541 nm. Scanning electron microscopy (SEM; XL-30 ESEM FEG, Micro FEI Philips) and transmission electron microscopy (TEM; JEOL JEM-2100) were employed to observe the morphologies and structures of the samples. Energy dispersive X-ray (EDX) spectroscopy being attached to scanning electron microscopy (SEM) was used to analyze the composition of products. Fourier transform infrared (FT-IR) spectra were recorded on a Magna 560 FT-IR spectrometer with a resolution of 1 cm^{-1}. X-ray photoelectron spectroscopy (XPS) was carried out on a VG-ESCALAB LKII instrument with a Mg Kα ADES ($h\nu = 1253.6$ eV) source at a residual gas pressure below 10^{-8} Pa. UV-vis diffuse reflectance spectra (DRS) were taken with a Lambda 750 UV/Vis/NIR spectrophotometer (Perkin Elmer, USA). The specific surface areas of the products were measured with a Micromeritics ASAP-2020 instrument and analyzed by the Brunauer–Emmett–Teller (BET) method. Decay curves of the as-fabricated products were obtained on a FLS920 fluorescence lifetime spectrophotometer (Edinburgh Instruments, UK) under the excitation of a hydrogen flash lamp with the wavelength at 325 nm (nF900; Edinburgh Instruments). The surface photovoltage spectroscopy (SPS) was performed on PL-SPS1000 instrument (Beijing Perfectlight Technology Co., Ltd). During the process, the sample was put between the indium tin oxide (ITO) glass and stainless steel electrodes to form a sandwich structured photovoltage cell.

Photocatalytic H_2 production. The photocatalytic H_2 production tests were performed in a 35-mL quartz reactor. Typically, 5 mg of the as-synthesized samples were suspended in 10-mL triethanolamine (TEOA, 15 vol.%) aqueous solution. This suspension was sealed in the quartz reactor by a rubber plug, and then purged with argon gas for half an hour to drive away the residual air. Subsequently, the reactor was exposed under a 300-W Xe lamp (PLS-SXE300UV) coupled with a 400 nm cut-off filter. The gas product composition from the upper space above the liquid in the quartz reactor was periodically analyzed by a gas chromatograph (GC) equipped with a thermal conductivity detector (TCD) (Beifen-Ruili Analytical Instrument, SP-3420A). The apparent quantum efficiency (QE) was estimated by using the following equation.

$$\mathrm{AQE} = \frac{2 \times number\ of\ evolved\ hydrogen\ molecules}{number\ of\ incident\ photons} \times 100\%$$

References

1. Liu, J. *et al.* Metal-free efficient photocatalyst for stable visible water splitting via a two-electron pathway. *Science* **347,** 970–974 (2015).
2. Jing, L., Zhou, W., Tian G. & Fu, H. Surface tuning for oxide-based nanomaterials as efficient photocatalysts. *Chem. Soc. Rev.* **42,** 9 509–9549 (2013).
3. Ran, J., Zhang, J., Yu, J., Jaroniec, M. & Qiao, S. Z. Earth-abundant cocatalysts for semiconductor-based photocatalytic water splitting. *Chem.Soc.Rev.* **43,** 7787–7812 (2014).
4. Ma, Y. *et al.* Titanium Dioxide-Based Nanomaterials for Photocatalytic Fuel Generations. *Chem. Rev.* **114,** 9987–10043 (2014).
5. Yu J. & Ran, J. Facile preparation and enhanced photocatalytic H_2-production activity of $Cu(OH)_2$ cluster modified TiO_2. *Energy Environ. Sci.* **4,** 1364–1371 (2011).
6. Manikandan, M. *et al.* Photocatalytic Water Splitting under Visible Light by Mixed-Valence Sn_3O_4. *ACS Appl. Mater. Interfaces* **6,** 3790–3793 (2014).
7. Zhang, J. *et al.* Efficient Visible-Light Photocatalytic Hydrogen Evolution and Enhanced Photostability of Core/Shell CdS/g-C_3N_4 Nanowires. *ACS Appl. Mater. Interfaces* **5,** 10317–10324 (2013).
8. Sun, S. Recent advances in hybrid Cu_2O-based heterogeneous nanostructures. *Nanoscale* **7,** 10850–10882 (2015).
9. Yu, C., Li, G., Kumar, S., Yang, K. & Jin, R. Phase transformation synthesis of novel Ag_2O/Ag_2CO_3 heterostructures with high visible light efficiency in photocatalytic degradation of pollutants, *Adv. Mater.*, **26,** 892–898 (2014).
10. Liu, Y., Zhang, M., Li, L. & Zhang, X. One-dimensional visible-light-driven bifunctional photocatalysts based on $Bi_4Ti_3O_{12}$ nanofiber frameworks and Bi_2XO_6 (X = Mo, W) nanosheets. *Appl. Catal. B* **160–161,** 757–766 (2014).
11. Wang, X. *et al.* A metal-free polymeric photocatalyst for hydrogen production from water under visible light. *Nature Chem.* **8,** 76–80 (2009).
12. Wang, R. *et al.* Quasi-Polymeric Metal-Organic Framework UiO-66/g-C_3N_4 Heterojunctions for Enhanced Photocatalytic Hydrogen Evolution under Visible Light Irradiation. *Adv. Mater. Interfaces* 10.1002/admi.201500037 (2015).
13. Yuan, Y.-P. *et al.* Improving photocatalytic hydrogen production of metal-organic framework UiO-66 octahedrons by dye-sensitization. *Appl. Catal. B* **168–169,** 572–576 (2015).
14. Han, X.-B. *et al.* Polyoxometalate-Based Nickel Clusters as Visible Light-Driven Water Oxidation Catalysts. *J. Am. Chem. Soc.* **137,** 5486–5493 (2015).
15. Cao, S. & Yu, J. G-C_3N_4-Based Photocatalysts for Hydrogen Generation. *J. Phys. Chem. Lett.* **5,** 2101–2107 (2014).
16. Yuan, Y.-P. *et al.* Microwave-assisted heating synthesis: a general and rapid strategy for large-scale production of highly crystalline g-C_3N_4 with enhanced photocatalytic H_2 production. *Green Chem.* **16,** 4663–4668 (2014).
17. Cao, S., Low, J., Yu, J. & Jaroniec, M. Polymeric Photocatalysts Based on Graphitic Carbon Nitride. *Adv. Mater.* **27,** 2150–2176 (2015).
18. Niu, P., Yin, L., Yang, Y., Liu, G. & Cheng, H. Increasing the Visible Light Absorption of Graphitic Carbon Nitride (Melon) Photocatalysts by Homogeneous Self-Modification with Nitrogen Vacancies. *Adv. Mater.* **26,** 8046–8052 (2014).
19. Kang, Y. *et al.* An Amorphous Carbon Nitride Photocatalyst with Greatly Extended Visible-Light-Responsive Range for Photocatalytic Hydrogen Generation. *Adv. Mater.* **27,** 4572–4577 (2015).
20. Cao, S.-W. *et al.* Artificial photosynthetic hydrogen evolution over g-C_3N_4 nanosheets coupled with cobaloxime. *Phys. Chem. Chem. Phys.* **15,** 18363–18366 (2013).
21. Zhang, Z., Huang, J., Zhang, M., Yuan, Q. & Dong, B. Ultrathin hexagonal SnS_2 nanosheets coupled with g-C_3N_4 nanosheets as 2D/2D heterojunction photocatalysts toward high photocatalytic activity. *Appl. Catal. B* **163,** 298–305 (2015).
22. Zhang, Z., Huang, J., Yuan Q. & Dong, B. Intercalated graphitic carbon nitride: a fascinating two-dimensional nanomaterial for an ultra-sensitive humidity nanosensor. *Nanoscale* **6,** 9250–9256 (2014).
23. Yuan, Y.-P., Cao, S.-W., Liao, Y.-S., Yin, L.-S. & Xue, C. Red phosphor/g-C_3N_4 heterojunction with enhanced photocatalytic activities for solar fuels production. *Appl. Catal. B*, **140–141,** 164–168 (2013).
24. Li, X. *et al.* Engineering heterogeneous semiconductors for solar water splitting. *J. Mater. Chem. A* **3,** 2485–2534 (2015).
25. Ye, L., Fu, J., Xu, Z., Yuan, R. & Li, Z. Facile One-Pot Solvothermal Method to Synthesize Sheet-on-Sheet Reduced Graphene Oxide (RGO)/$ZnIn_2S_4$ Nanocomposites with Superior Photocatalytic Performance. *ACS Appl. Mater. Interfaces* **6,** 3483–3490 (2014).
26. Zhang, P. *et al.* Bi_2MoO_6 ultrathin nanosheets on ZnTiO3 nanofibers: A 3D open hierarchical heterostructures synergistic system with enhanced visible-light-driven photocatalytic activity. *J. Hazard. Mater.* **217–218,** 422–428 (2012).
27. Liu, Y., Zhang, M. Y., Li L. & Zhang, X. T. One-dimensional visible-light-driven bifunctional photocatalysts based on $Bi_4Ti_3O_{12}$ nanofiber frameworks and Bi_2XO_6 (X = Mo, W) nanosheets. *Appl. Catal. B* **160–161,** 757–766 (2014).

28. Chen, Y. *et al.* Exploring the Different Photocatalytic Performance for Dye Degradations over Hexagonal $ZnIn_2S_4$ Microspheres and Cubic $ZnIn_2S_4$ Nanoparticles. *ACS Appl. Mater. Interfaces* **4,** 2273–2279 (2012).
29. Zhou, J. *et al. In situ* controlled growth of $ZnIn_2S_4$ nanosheets on reduced graphene oxide for enhanced photocatalytic hydrogen production performance. *Chem. Commun.* **49,** 2237–2239 (2013).
30. Shang, L. *et al.* Facile synthesis of hierarchical $ZnIn_2S_4$ submicrospheres composed of ultrathin mesoporous nanosheets as a highly efficient visible-light-driven photocatalyst for H_2 production. *J. Mater. Chem. A* **1,** 4552–4558 (2013).
31. Chen, Y. *et al.* Hierarchical Core−Shell Carbon Nanofiber@$ZnIn_2S_4$ Composites for Enhanced Hydrogen Evolution Performance. *ACS Appl. Mater. Interfaces* **6,** 13841–13849 (2014).
32. Mandal, L., Chaudhari, N. S. & Ogale, S. Self-Powered UV-vis Photodetector Based on $ZnIn_2S_4$/Hydrogel Interface. *ACS Appl. Mater. Interfaces* **5,** 9141–9147 (2013).
33. Liu, Q. *et al.* 2D $ZnIn_2S_4$ Nanosheet/1D TiO_2 Nanorod Heterostructure Arrays for Improved Photoelectrochemical Water Splitting. *ACS Appl. Mater. Interfaces* **6,** 17200–17207 (2014).
34. Zhang, Z. *et al.* Multichannel-Improved Charge Carrier Dynamics in Well-Designed Hetero-Nanostructural Plasmonic Photocatalysts Toward Highly Efficient Solar-to-Fuels Conversion. *Adv. Mater*. **27,** 5906–5914 (2015).
35. Wang, X., Chen, X., Thomas, A., Fu, X. & Antonietti, M. Metal-Containing Carbon Nitride Compounds: A New Functional Organic-Metal Hybrid Material. *Adv. Mater.* **21,** 1609–1612 (2009).
36. Liu, J., Zhang, T., Wang, Z., Dawson, G. & Chen, W. Simple pyrolysis of urea into graphitic carbon nitride with recyclable adsorption and photocatalytic activity. *J. Mater. Chem.* **21,** 14398–14401 (2011).
37. Zhang, Z. *et al.* Electrospun Nanofibers of p-Type NiO/n-Type ZnO Heterojunctions with Enhanced Photocatalytic Activity. *ACS Appl. Mater. Interfaces* **2,** 2915–2923 (2010).
38. Zhang, Z. *et al.* Hierarchical assembly of ultrathin hexagonal SnS_2 nanosheets onto electrospun TiO_2 nanofibers: enhanced photocatalytic activity based on photoinduced interfacial charge transfer. *Nanoscale* **5,** 606–618 (2013).
39. Li, X. H. *et al.* Local chemical states and thermal stabilities of nitrogen dopants in ZnO film studied by temperature-dependent x-ray photoelectron spectroscopy. *Appl. Phys. Lett.* **95,** 191903 (2009).
40. Xiang, Q., Yu, J. & Jaroniec, M. Preparation and Enhanced Visible-Light Photocatalytic H_2-Production Activity of Graphene/C_3N_4 Composites. *J. Phys. Chem. C* **115,** 7355–7363 (2011).
41. Cao, S.-W. *et al. In-situ* growth of CdS quantum dots on g-C_3N_4 nanosheets for highly efficient photocatalytic hydrogen generation under visible light irradiation. *Int. J. Hydrogen Energy* **38,** 1258–1266 (2013).
42. Cao, S.-W. *et al.* Solar-to-fuels conversion over In_2O_3/g-C_3N_4 hybrid photocatalysts. *Appl. Catal. B* **147,** 940–946 (2014).
43. Wang, X. *et al.* Engineering Interfacial Photo-Induced Charge Transfer Based on Nanobamboo Array Architecture for Efficient Solar-to-Chemical Energy Conversion. *Adv. Mater.* **27,** 2207–2214 (2015).
44. Chen, Y.-C., Pu, Y.-C. & Hsu, Y.-J. Interfacial Charge Carrier Dynamics of the Three-Component In_2O_3-TiO_2-Pt Heterojunction System. *J. Phys. Chem. C* **116,** 2967–2975 (2012).
45. Bian, Z., Tachikawa, T., Kim, W., Choi, W. & Majima, T. Superior Electron Transport and Photocatalytic Abilities of Metal-Nanoparticle-Loaded TiO_2 Superstructures. *J. Phys. Chem. C* **116,** 25444–25453 (2012).
46. Yang, T.-T. *et al.* Interfacial Charge Carrier Dynamics in Core-Shell Au-CdS Nanocrystals. *J. Phys. Chem. C* **114,** 11414–11420 (2010).

Acknowledgements

This work is supported by the National Natural Science Foundation of China (grant nos 51402038, 11474046, and 11274057), Program for New Century Excellent Talents in University (NCET-13-0702), Technology Foundation for Selected Overseas Chinese Scholar from Ministry of Personnel of China, Scientific Research Foundation for Doctor of Liaoning Province (grant no. 20141118), Educational Committee Foundation of Liaoning Province (grant no. L2014547), Science and Technology Project of Liaoning Province (grant no. 2012222009), Program for Liaoning Excellent Talents in University (LNET) (grant no. LJQ2012112), Fundamental Research Funds for the Central Universities (grant nos DC201502080203 and DC201502080304), and Science and Technique Foundation of Dalian (grant no. 2013A14GX040).

Author Contributions

Z.Z. and B.D. proposed and guided the overall project. Z.Z. carried out the major part of experiments and results analyses. K.L., Z.F. and Y.B. assisted Z.Z. to perform the materials characterizations. Z.Z. wrote the manuscript with discussion from all authors. All authors reviewed the manuscript.

Additional Information

Supplementary information accompanies this paper at http://www.nature.com/srep

Competing financial interests: The authors declare no competing financial interests.

How to cite this article: Zhang, Z. *et al.* Hierarchical Sheet-on-Sheet $ZnIn_2S_4$/g-C_3N_4 Heterostructure with Highly Efficient Photocatalytic H_2 production Based on Photoinduced Interfacial Charge Transfer. *Sci. Rep.* **6**, 19221; doi: 10.1038/srep19221 (2016).